Journal of Japan Association for Earthquake Engineering, Vol. 25, No. 8, 2025

INTERNAL DAMAGE DETECTION FOR RUBBER BEARINGS USING MACHINE LEARNING METHODS

Kohei MORIKAWA[1], Yuma KAWASAKI[2], Yasutoshi NOMURA[3] and Kazuyuki IZUNO[4]

[1] M. Eng., Former Graduate Student, Graduate School of Ritsumeikan University /
Oriental Consultants Co., Ltd., Osaka, Japan, morikawa-k@oriconsul.com
[2] Member, Dr. Eng., Associate Professor, Department of Civil and Environmental Engineering,
Ritsumeikan University, Shiga, Japan, yuma-k@fc.ritsumei.ac.jp
[3] Dr. Informatics, Professor, Department of Civil and Environmental Engineering,
Ritsumeikan University, Shiga, Japan, y-nomura@fc.ritsumei.ac.jp
[4] Member, Dr. Eng., Department of Civil and Environmental Engineering,
Ritsumeikan University, Shiga, Japan, izuno@se.ritsumei.ac.jp

ABSTRACT: Rubber bearings are now commonly used to prevent seismic damage to bridges; however, they can be destroyed by a major earthquake. Even if the bearing is not completely destroyed, it may sustain internal damage. Such internal damage is difficult to detect because they have a rubber coating. By conducting a numerical analysis, this study verified the propagation of elastic waves in a laminated rubber bearing, and used the data to detect damage using a machine learning anomaly detection technique. The results showed that damage inside a rubber bearing can be detected using the one-class support vector machine anomaly detection method.

Keywords: *Bridge, Rubber bearing, Machine learning, Anomaly detection, Internal damage*

1. INTRODUCTION

Since the 1995 Kobe Earthquake, it has become common to install rubber bearings in Japan's bridges. They are often used because their seismic resistance is superior to metal bearings. However, it is difficult to visually inspect the internal state of these bearings because they have a rubber coating.

During the 2011 off the Pacific coast of Tohoku Earthquake and the 2016 Kumamoto Earthquake, the rubber bearings ruptured and were replaced during the subsequent restoration work1)–3). However, it is difficult to determine the necessity of replacing a bearing which has not ruptured in spite of its vicinity to ruptured bearings.

When a rubber bearing ruptures, the Handbook on Laminated Rubber Bearings4) states that the deformation increases abruptly because "the steel plates on the top and bottom restrain the deformation of the rubber to keep the volume of the rubber constant in response to tensile deformation, resulting in a negative pressure inside the rubber, causing the air contained inside the rubber to appear as voids and reducing its apparent cross-sectional area." Therefore, the early detection of voids inside the rubber layer would facilitate assessment of the condition of the rubber bearing.

Regarding the health and deterioration of rubber bearings, Usami et al.5) estimated the service life based on accelerated deterioration tests, Ito et al.[6), 7)] conducted a series of studies on ozone deterioration, and Hayashi et al.[8), 9)] conducted a study on the residual performance of actual aged rubber bearings. However, none of these methods can be applied to the nondestructive detection of internal voids. The authors have conducted experiments to detect the presence of small voids inside rubber bearings by applying the acoustic emission (AE) method[10)–14)], but numerous experiments still need to be conducted to generalize the conclusions.

Therefore, in the area of abnormality detection, this study attempted to detect internal voids using a machine learning method. Numerical models of a healthy rubber bearing and a rubber bearing with internal voids were created, and a large number of numerical analyses simulating the impact elastic wave tests were conducted to accumulate data. This paper assumes that a bearing underwent large deformation due to an earthquake, and focuses on internal damage that cannot be detected by visual inspection, unlike cracks caused by ozone degradation.

2. NUMERICAL ANALYSIS METHODS

The governing Eqs. for a 3-D dynamic elasticity problem assuming linear micro-deformation are expressed in Eqs. (1) to (9).

$$\partial_t v_x = \left(\partial_x \sigma_{xx} + \partial_y \sigma_{xy} + \partial_z \sigma_{zx}\right)/\rho \tag{1}$$

$$\partial_t v_y = \left(\partial_y \sigma_{yy} + \partial_z \sigma_{yz} + \partial_x \sigma_{xy}\right)/\rho \tag{2}$$

$$\partial_t v_z = \left(\partial_z \sigma_{zz} + \partial_x \sigma_{zx} + \partial_y \sigma_{yz}\right)/\rho \tag{3}$$

$$\partial_t \sigma_{xx} = (\lambda + 2\mu)\partial_x v_x + \lambda \partial_y v_y + \lambda \partial_z v_z \tag{4}$$

$$\partial_t \sigma_{yy} = \lambda \partial_x v_x + (\lambda + 2\mu)\partial_y v_y + \lambda \partial_z v_z \tag{5}$$

$$\partial_t \sigma_{zz} = \lambda \partial_x v_x + \lambda \partial_y v_y + (\lambda + 2\mu)\partial_z v_z \tag{6}$$

$$\partial_t \sigma_{yz} = \mu \partial_z v_y + \mu \partial_y v_z \tag{7}$$

$$\partial_t \sigma_{zx} = \mu \partial_x v_z + \mu \partial_z v_x \tag{8}$$

$$\partial_t \sigma_{xy} = \mu \partial_y v_x + \mu \partial_x v_y \tag{9}$$

where the subscripts denote direction, v is the displacement velocity, σ is the stress, λ and μ are Lame's constants, ρ is the density, ∂_t is the partial derivative with respect to time *t*, and ∂_x, ∂_y and ∂_z are partial derivatives with respect to space in each direction.

These are separated in each direction, and the method of characteristics is further applied to obtain a one-dimensional advection equation[15)]. For example, Eqs. (10) to (15) are shown for the x direction.

$$\partial_t \left(v_x \mp \frac{\sigma_{xx}}{c_L \rho}\right) \pm c_L \partial_x \left(v_x \mp \frac{\sigma_{xx}}{c_L \rho}\right) \pm \left(v_x \mp \frac{\sigma_{xx}}{c_L \rho}\right) \partial_x c_L = 0 \tag{10}$$

$$\partial_t \left(v_y \mp \frac{\sigma_{xy}}{c_T \rho}\right) \pm c_T \partial_x \left(v_y \mp \frac{\sigma_{xy}}{c_T \rho}\right) \pm \left(v_y \mp \frac{\sigma_{xy}}{c_T \rho}\right) \partial_x c_T = 0 \tag{11}$$

$$\partial_t \left(v_z \mp \frac{\sigma_{zx}}{c_T \rho}\right) \pm c_T \partial_x \left(v_z \mp \frac{\sigma_{zx}}{c_T \rho}\right) \pm \left(v_z \mp \frac{\sigma_{zx}}{c_T \rho}\right) \partial_x c_T = 0 \tag{12}$$

$$\partial_t\left(\sigma_{yy}-\frac{\lambda}{\lambda+2\mu}\sigma_{xx}\right)=0 \tag{13}$$

$$\partial_t\left(\sigma_{zz}-\frac{\lambda}{\lambda+2\mu}\sigma_{xx}\right)=0 \tag{14}$$

$$\partial_t\sigma_{yz}=0 \tag{15}$$

where, $c_L=\sqrt{\frac{\lambda+2\mu}{\rho}}$, $c_T=\sqrt{\frac{\mu}{\rho}}$, and the double signs in Eqs. (10) to (12) are in the same order.

Equations (10) to (12) are the advection equations due to the longitudinal wave velocity c_L and transverse wave velocity c_T, respectively. This study uses the CIP method to solve these equations. The CIP method considers that the spatial derivative of a variable is also advected, but the partial derivative in the other direction is required when calculating the advection in each direction. For example, in the calculation of the x-direction, the M-type CIP method[16), 17)] is used to calculate the partial derivatives in the y- and z-directions by using the central difference in space. The above procedure was repeated for the y- and z-directions.

To reduce wave reflections at the boundary, a perfectly matched layer (PML) absorbing boundary[18)] was used. This is a boundary where a virtual computational grid is set outside the computational domain to allow propagating waves to decay gradually, and is a method often used in wave propagation problems.

3. ANALYSIS MODEL

The analytical model is based on the specimen used in the experiment by Nose et al.[19)] and is a rectangular body of $180\times106\times180$ mm. The material properties of rubber shown in Table 1, obtained from the same experiment, were also used in the numerical analysis of this study. For steel plates, elastic wave velocities calculated from Young's modulus and Poisson's ratio in the specifications for highway bridges were used. Figure 1 shows the coordinate axes set for the analytical model and Fig. 2 shows a cross-sectional view. This is assumed to be a model of a healthy bearing. Due to the performance limitations of the PC used, the analytical mesh was a cube with 1 mm sides. The maximum amplitude of the observed waveforms differs by about 6% compared to a cubic mesh of 2 mm per side, indicating a certain degree of grid convergence.

Next, a specimen with an internal void was modeled. Damage to the laminated rubber bearing is often caused by large tensile stresses near the edges of the upper and lower steel plates[20), 21)]. Therefore, a void simulating imaginary damage was set in the rubber layer between the top steel plate and the top inner steel plate. To see the effect of position, voids were created at the six positions shown in Fig. 3. The void size was $30\times2\times30$ mm. A total of six models with internal voids were prepared, with one void from L1 to L6, respectively. Though the internal voids may occur anywhere in the rubber layer, this study was conducted with a limited number of internal void positions, as shown in Fig. 3. This was because the main purpose was to confirm whether the proposed method can detect internal voids or not.

Table 1 Assumed material properties

	Longitudinal wave velocity (m/s)	Transverse propagation velocity (m/s)	Poisson's ratio	Density (kg/m^3)
Rubber	1600	30	0.49986	1140
Steel plate	5900	3200	0.3	7850

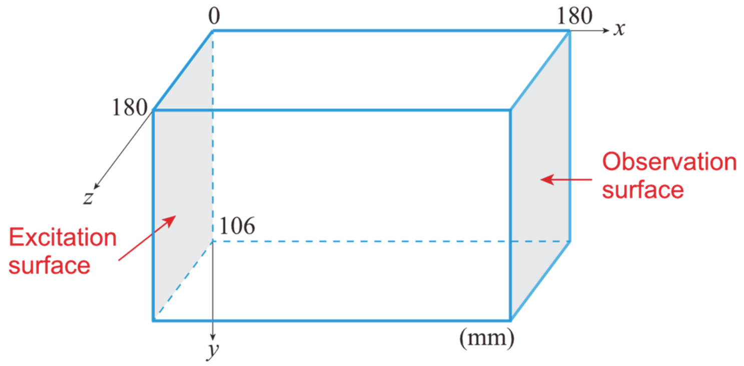

Fig. 1 Coordinate axes set in the analysis model

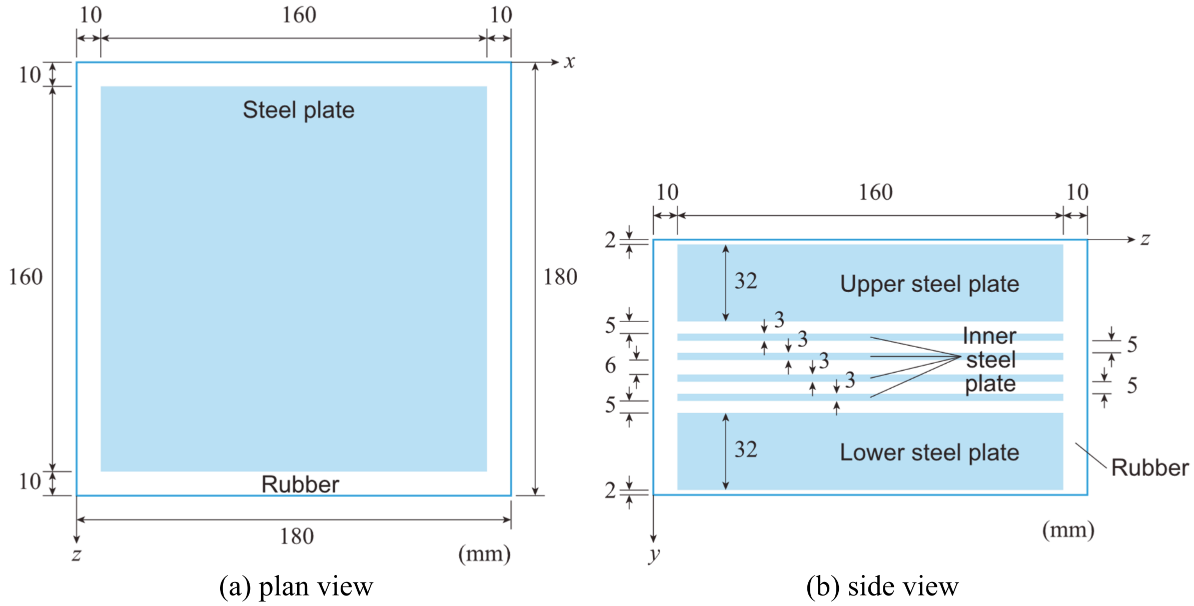

(a) plan view (b) side view

Fig. 2 Cross-sectional view of healthy bearing model

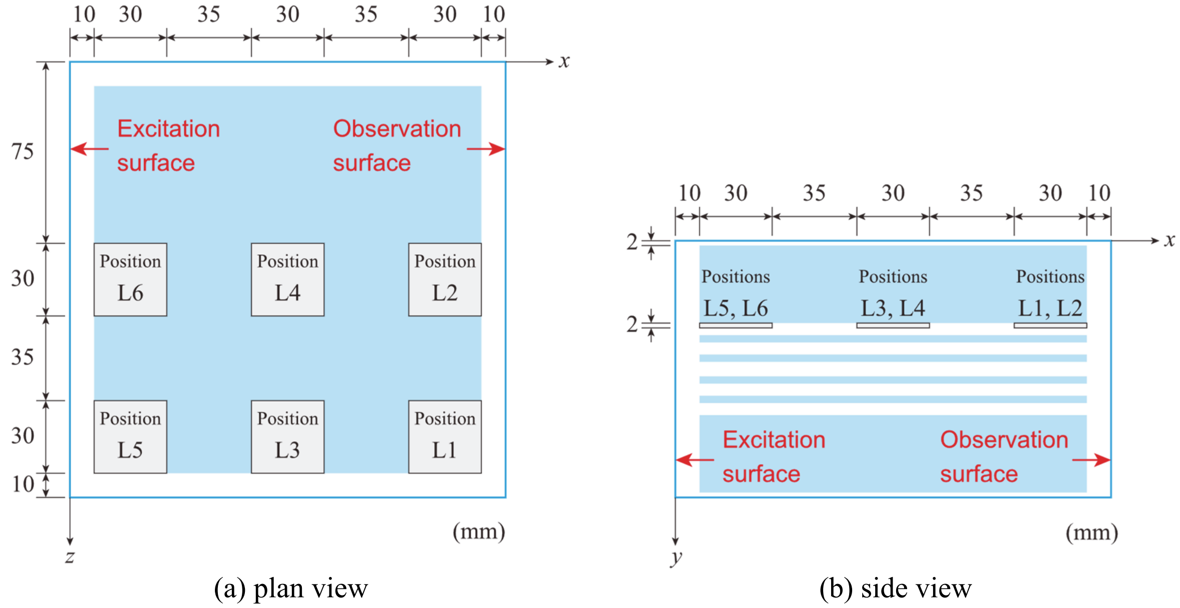

(a) plan view (b) side view

Fig. 3 Cross-sectional view of bearing model with internal void and void position

The excitation was applied to a circle of radius $r_0 = 10$ mm centered at the excitation point $(0, y_0, z_0)$, with a maximum excitation force at the center point and spatially decreasing in accordance with the cosine curve as the initial condition at $t = 0$. The reason for using a smooth condition with a wide range instead of point excitation was to obtain as stable a numerical solution as possible. The maximum value of the excitation force was set to 1 N.

Excited elastic waves propagate through the rubber and steel layers and reach the observation point. The transmission rate from the rubber layer to the steel plate layer or from the steel plate layer to the rubber layer is calculated from the difference in the acoustic impedance of each layer. Using the values in Table 1, 8% of the elastic waves are transmitted to the other layer and 92% are reflected. Further, the boundary with the inner void is assumed to be 100% reflective. Experiments by the authors14) have confirmed that the elastic wave transmitted through the rubber layer can be observed with high accuracy.

4. ANOMALY DETECTION METHOD USING MACHINE LEARNING

This study used the one-class support vector machine22) (OCSVM) as an anomaly detection method. OCSVM is often used as an unsupervised machine learning method to determine whether unknown data is normal or abnormal by learning the distribution range of data mapped to the feature space using data that is mostly normal. There is also a way of using this OCSVM for supervised machine learning, in which only normal data are used as training data to be learned. If unknown data deviates from the distribution, it is judged to be novel and an anomaly can be detected. This study employed the latter method, in which waveforms obtained from a healthy model were used as training data. A novelty rating means that the targeted bearing has different characteristics from a healthy bearing, suggesting the presence of internal voids. The library function “fitcsvm” in MATLAB was used, and the Gaussian kernel was utilized. If the anomaly score of the validation data computed by the function “fitcsvm” is less than or equal to 0, it is evaluated as a novelty.

In the following analysis, 36 positions $(9\ \text{rows} \times 4\ \text{columns} = 36)$ were set on the excitation surface shown in Fig. 4, and elastic waves were collected at 40 observation points $(5\ \text{rows} \times 8\ \text{columns} = 40)$ shown in Fig. 5, for a total of $36 \times 40 = 1{,}440$ waves during an interval of 0.8 ms after excitation. Because the amplitude of the observed wave differs depending on the positional relationship between the excitation and observation points, the amplitude was adjusted so that the maximum amplitude of each waveform was 1.

The features described as follows were calculated for the waveforms of these healthy bearing models, and these were used as healthy training data for machine learning. The following parameters, which are commonly used in anomaly detection, were selected as the feature values: [1] mean, [2] variance, [3] root mean square, [4] maximum amplitude, [5] skewness, [6] kurtosis, [7] to [10] mean, variance, skewness, and kurtosis of spectral kurtosis, [11] the number of times that 1/100 of the peak amplitude is recorded (the value of 1/100 is set by trial), [12] to [16] the frequencies of the first to fifth largest peaks of the Fourier amplitude, [17] to [21] the phase angle corresponds to [12] to [16], and [22] to [26] the frequencies of the first to fifth largest peaks of the Fourier amplitude sorted in order of magnitude.

Next, using a bearing model with an internal void at one of the positions L1 to L6 shown in Fig. 3, the model was subjected to excitation at the 10 points indicated by the red dots in Fig. 6, and the features were calculated from waveforms observed at the same 40 points as those of the healthy bearing. The 40 observation points are marked with a symbol from S1 to S40 from the left of the Fig. in each row as shown in Fig. 7. Figures 6 and 7 also show the position of the internal void in the *y*-*z* plane.

Examples of the obtained waveforms and their Fourier spectra are shown in Figs. 8 and 9. These figures show the waves observed at S29 in Fig. 7 when the bearing model with an internal void at L6 is excited at E9 in Fig. 6. The waveforms obtained from the healthy bearing model and the bearing model with an internal void show little difference in terms of both the time history waveforms and the Fourier spectra.

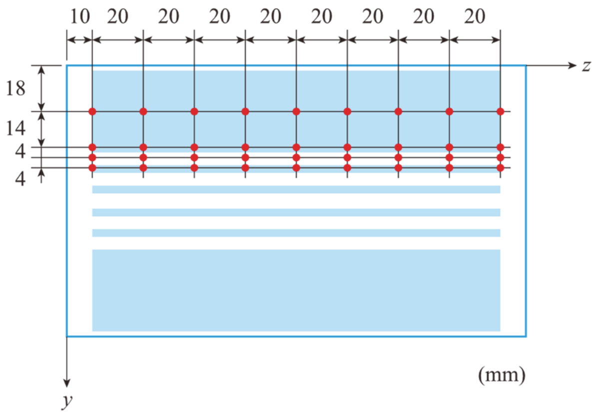

Fig. 4 Excitation surface of healthy bearing
$(x = 0)$

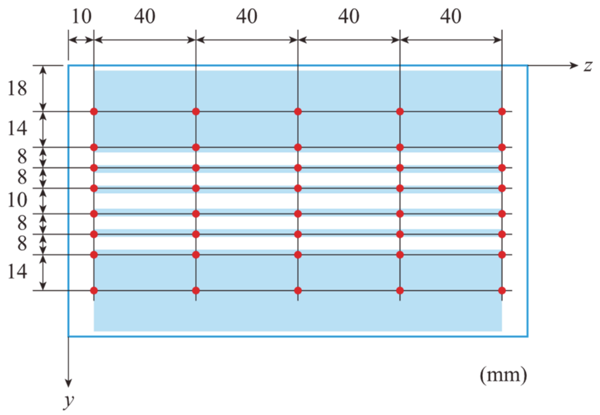

Fig. 5 Observation surface of healthy bearing
$(x = 180\ \text{mm})$

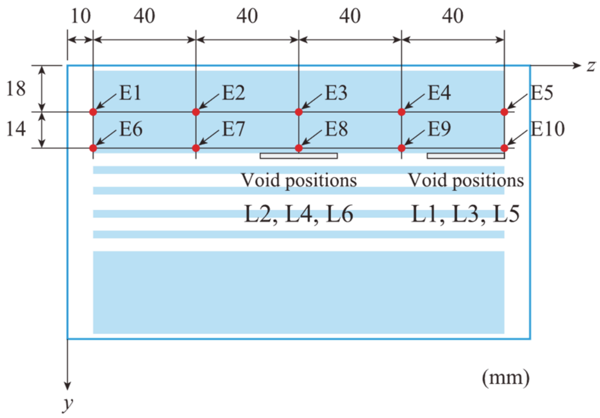

Fig. 6 Excitation point number
for bearing with an internal void

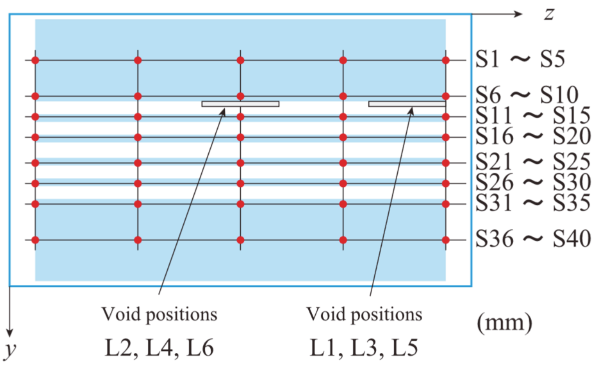

Fig. 7 Observation point number
for bearing with an internal void

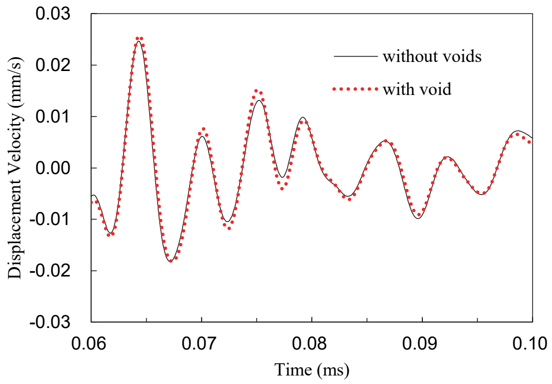

Fig. 8 Examples of observed time history waveforms

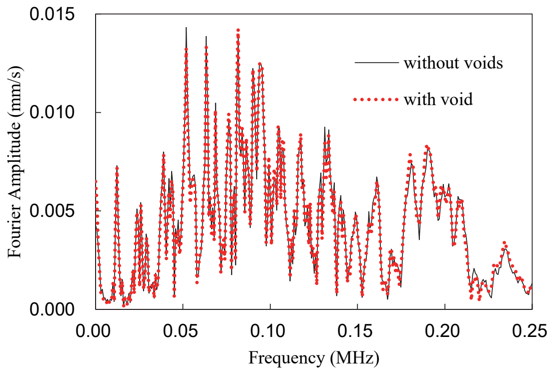

Fig. 9 Example of Fourier spectrum

The maximum amplitude in Fig. 8 and the dominant frequency in Fig. 9 do not differ significantly from the healthy model. This is due to the fact that the maximum is mainly affected by the direct waves. The difference from the healthy model is caused by the reflection of elastic waves at the boundary between the inner void and the rubber or steel plate, and interference with the propagating waves. The presence or absence of an internal void is difficult to determine by a simple comparison of maximum values, etc. The next chapter details how to describe the presence or absence of internal voids using machine learning.

5. INTERNAL VOID DETECTION RESULTS

The novelty of the validation data is indicated in MATLAB by a histogram of outlier scores as shown in Fig. 8. This histogram plots the frequency distribution of the anomaly scores calculated from the wave features recorded at all observation points by the excitation at a single position, expressed as a relative probability so that the sum is 1. Figure 10(a) is a histogram of anomaly scores calculated from the waves recorded at all observation points in Fig. 7 when the bearing model with the aforementioned internal void at L6 was excited at E9 in Fig. 6. All score values in the training data computed for the healthy bearing model are greater than or equal to 0, whereas the validation data has values less than the threshold value of 0, indicating that the model is novel. Thus, it is possible to detect internal voids from the histogram of anomaly scores.

On the other hand, the histogram calculated from the observed waves when the bearing model with the aforementioned internal void at L6 was excited at E1 in Fig. 6 is shown in Fig. 10(b). This figure shows that a void is not considered to exist inside, indicating that a void may not be detectable depending on the position of the excitation point. This is due to the positional relationship between the excitation point E1 and the void position L6. In a real bearing, the position of the internal void is unknown, so the bearing must be excited at various points.

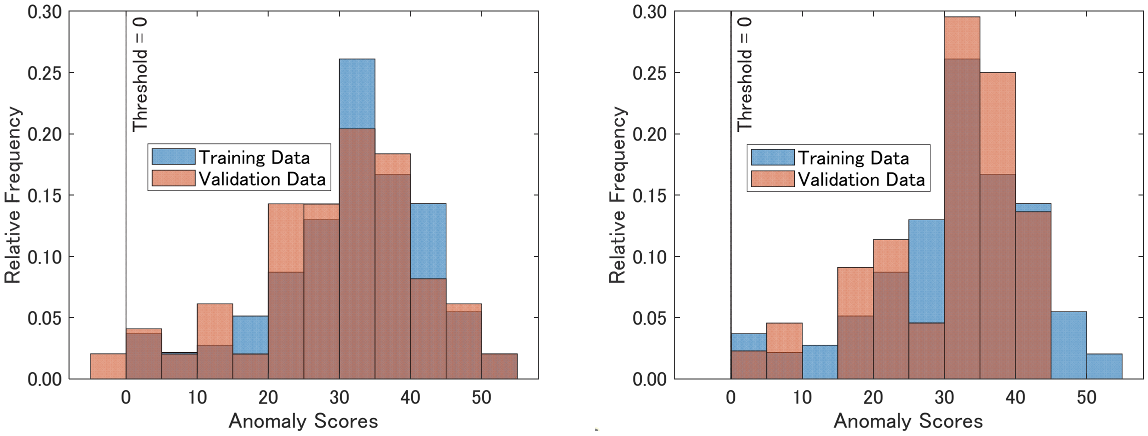

(a) Cases judged as novel

(b) Cases judged as not novel

Fig. 10 Histogram of anomaly score values

Table 2 Observations of records determined to be novel

		Excitation position									
		E1	E2	E3	E4	E5	E6	E7	E8	E9	E10
Void position	L1	×	×	×	×	×	×	×	×	×	×
	L2	×	S7	×	×	×	×	×	S28	S29	×
	L3	×	×	S8	×	×	×	S27	×	S29	S5
	L4	×	×	×	S9	×	×	×	S28	×	×
	L5	×	×	×	×	S10	×	×	×	S29	×
	L6	×	S7	×	×	×	×	S27	×	S29	×

Note that when the observed values for a healthy bearing were used as the validation data, no novelty was judged to exist. This shows that no false judgments were made.

The above shows that the positional relationship between the excitation position and the observation point determines whether the internal void can be detected by this method or not. Table 2 shows which data points were judged to have novelty in each case. For example, the record at observation point S29 was evaluated as novel with an anomaly score below 0 in Fig. 10(a). The symbol “×” indicates that there were no data evaluated as novel.

Table 2 shows that no record of novelty was found at the void position L1, which is far from the shaker surface, but this could be addressed by exciting another surface. For the void positions L2 to L6, waves recorded at observation points in the vertical plane perpendicular to the excitation surface passing through the excitation point (e.g., observation point S7 for excitation point E2, observation point S28 for excitation point E8) were judged to have novelty. Fig. 11 shows the positional relationship in the *y*-*z* plane of the excitation and observation points that were judged to have novelty. This figure shows that the novelty is evaluated at the excitation and observation points that are aligned vertically.

When the excitation was applied at the height of E1 to E5, which is near the center of the upper steel plate, the observation points of S7 to S10, which are near the bottom of the upper steel plate, were often judged to have novelty. This is thought to be the effect of waves reflected at the top of the inner void. When E6 to E10 and the lower part of the upper steel plate were excited, the observation points at the lower part of the bearing S27 to S29 were often judged to have novelty.

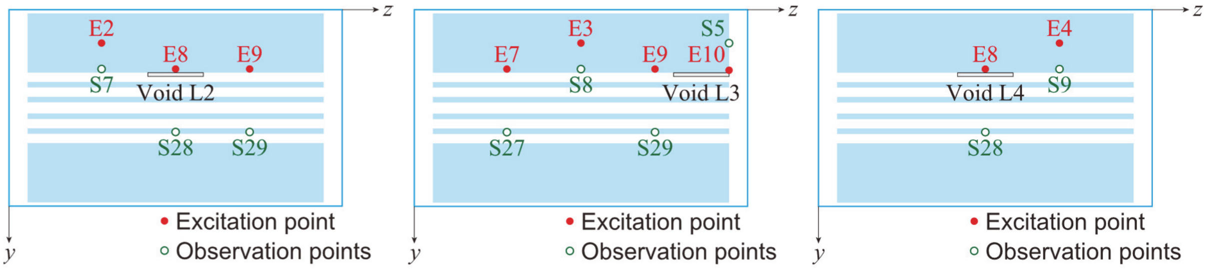

(a) Void position L2 (b) Void position L3 (c) Void position L4

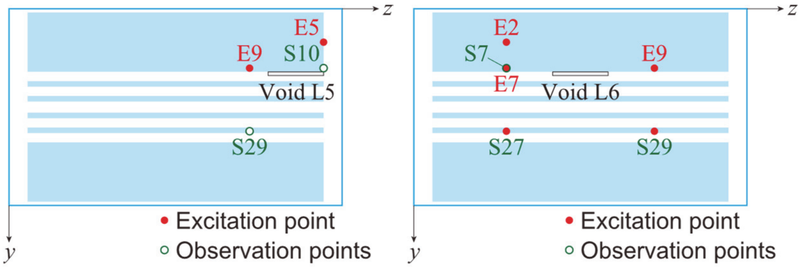

(d) Void position L5 (e) Void position L6

Fig. 11 Position of excitation and observation points judged to have novelty

Table 3 Observations of records determined to have novelty by assuming small voids

		Excitation position									
		E1	E2	E3	E4	E5	E6	E7	E8	E9	E10
Void position	L1	×	×	×	×	×	×	×	×	×	×
	L2	×	×	×	×	×	×	×	×	×	×
	L3	×	×	×	×	×	×	×	×	×	×
	L4	×	×	×	×	×	×	×	S3	×	×
	L5	×	S7	×	×	×	×	×	S3	S29	×
	L6	×	×	×	×	×	×	×	×	×	×

The internal voids may have the effect of diffracting elastic waves. The positional relationship between the excitation point and the observation point where the anomaly was detected is considered to be useful information for planning the placement of observation sensors when conducting future experiments and field measurements.

On the other hand, comparing the columns in Table 2, when there is no void in the vertical plane perpendicular to the excitation plane passing through the excitation point, such as at excitation points E1 and E6, there were no records judged to be novel. This also means that the actual bearing must be excited at several points because the position of the internal void is unknown.

Comparing the rows of Table 2, several excitation cases were judged to have novelty for the void positions L2 to L6. Therefore, it is predicted that the accuracy of detecting internal voids will be increased by exciting the bearing at several points.

Then, we ranked the features [1] to [26] by Laplacian score using the MATLAB library function “fsulaplacian” to ascertain what features were deemed important by OCSVM in determining novelty. The Laplacian scores all differed by only about 10^{-4}, almost 1, but the top four were the frequencies with the second to fifth largest Fourier amplitude peaks. As noted for Fig. 9, there is no significant difference in the predominant frequencies, and the difference is in which frequencies the second and subsequent waves were reached. Although it is necessary to examine more carefully what features should be used as effective features, this method is capable of detecting internal voids.

When the void size was reduced from $30 \times 2 \times 30$ mm to $5 \times 2 \times 5$ mm, the number of records judged to have novelty is shown in Table 3, which was fewer than the number in Table 2, suggesting that it is difficult to detect small voids. However, the size of the analytical mesh also affects the accuracy of the judgment. Further studies are needed to verify the method using experimental data, rather than numerical analysis data.

6. CONCLUSIONS

This study examined the determination of internal damage in rubber bearings using a machine learning anomaly detection method. One-class support vector machine (OCSVM) analysis was performed using data obtained by numerically modeling a healthy rubber bearing and a rubber bearing with internal voids and simulating the impact elastic wave method.

The propagation of elastic waves generated by excitation on the side of a healthy rubber bearing model was analyzed numerically, and the waves were observed at 40 positions on the opposite side. The features of the waveforms were machine-learned as healthy data. The same numerical analysis was performed for a rubber bearing model with an internal void, and OCSVM analysis was performed as validation data. The data from several excitation and observation points were determined to be novel in the validation data, and the presence of internal voids could be detected.

The results of OCSVM analysis with different positions of the internal void showed that the presence of the void could not be detected when the void was located far from the point of excitation. In the cases where detection was possible, the records of observation points in the vertical plane perpendicular to the excitation surface passing through the excitation point were valid.

ACKNOWLEDGMENT

The authors would like to express their gratitude to the JSPS Grant-in-Aid for Scientific Research JP20K04672.

REFERENCES

1) Soda, N., Yamada, K., Kimizu, T., Hirose, T. and Suzuki, M.: Performance Test of Natural Rubber Bearing Ruptured According to the 2011 off the Pacific Coast of Tohoku Earthquake, *Journal of Structural Engineering*, A, Vol. 59A, pp. 516–526, 2013 (in Japanese).
2) Shinohara, M. and Hoshikuma, J.: Experimental Evaluation of Property of Lead Rubber Bearing

Damaged Due to Earthquake, *Journal of Japan Society of Civil Engineers*, Ser. A1, Vol. 71, No. 4, pp. I_587–I_599, 2015 (in Japanese).

3) Takahashi, Y.: Damage of Bridges Caused by the 2016 Kumamoto Earthquake and Estimation of Failure Mechanism Based on Field Survey after Foreshock and Mainshock, *Journal of Japan Society of Civil Engineers*, Ser. A1, Vol. 73, No. 4, pp. I_225–I_235, 2017 (in Japanese).
4) Editorial Committee of Handbook of Laminated Rubber Bearings for Building Seismic Isolation: *Revised Handbook for Designers of Laminated Rubber Bearings for Building Base Isolation*, Japan Rubber Association and Japan Seismic Isolation Association, p. 335, 2017 (in Japanese).
5) Usami, T., Watanabe, M., Kitta, T., Yonehama, T., Hayashi, K. and Nagano, E.: Durability of Rubber Bearing Pads (I), *Nippon Gomu Kyokaishi*, Vol. 54, No. 3, pp. 174–184, 1981 (in Japanese).
6) Itoh, Y., Satoh, K., Gu, H. and Yamamoto, Y.: Study on the Long-Term Deterioration of Natural Rubber of Bridge Bearings, *Journal of Japan Society of Civil Engineers*, No. 801/I-73, pp. 801_185–801_196, 2005 (in Japanese).
7) Itoh, Y., Satoh, K., Gu, H. and Yamamoto, Y.: Study on the Deterioration Characteristics of Natural Rubber Bearings, *Journal of Japan Society of Civil Engineers*, Ser. A, Vol. 62, No. 2, pp. 255–266, 2006 (in Japanese).
8) Hayashi, K., Adachi, Y., Komoto, K., Yatsumoto, H., Igarashi, A., Dang, J. and Higashide, T.: Experimental Verification for Remaining Performance of Lead Rubber Bearings with Aging Deterioration, *Journal of Japan Society of Civil Engineers*, Ser. A1, Vol. 70, No. 4, pp. I_1032–I_1042, 2014 (in Japanese).
9) Hayashi, K., Adachi, Y., Sakamoto, N., Igarashi, A., Dang, J., Otani, O. and Shimoike, T.: Fundamental Analysis for Identifying Deterioration Mechanism of Lead Rubber Bearings, *Journal of Japan Society of Civil Engineers*, Ser. A1, Vol. 71, No. 4, pp. I_525–I_536, 2015 (in Japanese).
10) Kawasaki, Y., Teramura, N., Izuno, K. and Okada, S.: Using Acoustic Emissions to Assess Damage to Laminated Rubber Bearings, *Journal of Japan Society of Civil Engineers*, Ser. A1, Vol. 71, No. 2, pp. 244–254, 2015 (in Japanese).
11) Kawasaki, Y., Teramura, N. and Izuno, K.: Acoustic Emission Technique for Evaluation of Damage to Laminated Rubber Bearing, *Journal of Japan Society of Civil Engineers*, Vol. 5, No. 1, pp. 2–9, 2017. https://doi.org/10.2208/journalofjsce.5.1_2
12) Kawasaki, Y., Tanaka, A., Teramura, N., Ueda, K. and Izuno, K.: Accuracy Evaluation Test to Detect Peeling Healthy inside Rubber by AE Method, *Journal of Japan Society of Civil Engineers*, Ser. A1, Vol. 74, No. 2, pp. 241–250, 2018 (in Japanese).
13) Tanaka, A., Kawasaki, Y., Ueda, K. and Izuno, K.: Influence of Cyclic Shear Deformation on Ae Characteristics of Laminated Rubber Bearing, *Journal of Japan Society of Civil Engineers*, Ser. A1, Vol. 74, No. 4, pp. I_481–I_489, 2018 (in Japanese).
14) Kawasaki, Y., Ueda, K. and Izuno, K.: AE Source Location of Debonding Steel-Rod Inserted and Adhered inside Rubber, *Construction and Building Materials*, Vol. 279, 2021. https://doi.org/10.1016/j.conbuildmat.2021.122383
15) Saito, J.: An Application of the CIP Method to Elastodynamics, *Journal of Applied Mechanics*, Japan Society of Civil Engineers, Vol. 12, pp. 135–142, 2009 (in Japanese).
16) Yabe, T., Utsumi, T. and Ogata, Y.: *CIP Method*, Morikita Publishing, Tokyo, 2003 (in Japanese).
17) Nakamura T. and Yabe, T.: Cubic Interpolated Propagation Scheme for Solving Hyper-Dimensional Vlasov–Poisson Equation in Phase Space, *Computer Physics Communications*, Vol. 120, pp. 122–154, 1999. https://doi.org/10.1016/S0010-4655(99)00247-7
18) Collino, F. and Tsogka, C.: Application of the Perfectly Matched Absorbing Layer Model to the Linear Elastodynamics Problem in Anisotropic Heterogeneous Media, *Geophysics*, Vol. 66, No. 1, pp. 294–307, 2001. https://doi.org/10.1190/1.1444908
19) Nose, Y., Izuno, K. and Kawasaki, Y.: Numerical Simulation for Detecting Internal Void of Seismic Rubber Bearing, *Journal of Japan Association for Earthquake Engineering*, Vol. 20, No. 5, pp. 5_24–5_35, 2020. https://doi.org/10.5610/jaee.20.5_24
20) Kosugi, S., Imaoka, T., Kanazawa, K., Hiraki, T., Nagata, S., Nakayama, T., Sato, K., Jimbo, M. and Umeki, Y.: Ultimate Properties of Large-Scale Lead Rubber Bearing Using Full-Scale Break Test, *Journal of Structural and Construction Engineering* (*Transactions of AIJ*), Vol. 82, No. 732,

pp. 203–213, 2017 (in Japanese).

21) Choi, J., Sung, H., Hara, N., Imai, T. and Ueda, K.: FE Analyses of Experiments for Shear Properties of Rubber Bearings with Parameters of Axial Stress Parameters and Evaluation of Local Internal Stress of Rubber Bearings, *Journal of Japan Society of Civil Engineers*, Ser. A1, Vol. 74, No. 4, pp. I_795–I_802, 2018 (in Japanese).
22) MathWorks: Fit One-Class Support Vector Machine (SVM) Model for Anomaly Detection. https://www.mathworks.com/help/stats/ocsvm.html (last accessed on October 13, 2024)

(Original Japanese Paper Published: September, 2024)
(English Version Submitted: November 01, 2024)
(English Version Accepted: February 24, 2025)